OPEN ACCESS



MHD Inertial and Energy-containing Range Turbulence Anisotropy in the Young Solar Wind

Laxman Adhikari^{1,2}, Gary P. Zank^{1,2}, Lingling Zhao^{1,2}, Bingbing Wang², Bofeng Tang^{2,3}, Daniele Telloni⁴, Alexander Pitna⁵, and Katariina Nykyri⁶

Department of Space Science, University of Alabama in Huntsville, Huntsville, AL 35899, USA
 Center for Space Plasma and Aeronomic Research (CSPAR), University of Alabama in Huntsville, Huntsville, AL 35899, USA
 State Key Laboratory of Space Weather, National Space Science Center, Chinese Academy of Science, Beijing, 100190, People's Republic of China Anational Institute for AstrophysicsAstrophysical Observatory of Torino Via Osservatorio 20, I-10025 Pino Torinese, Italy Charles University, Faculty of Mathematics and Physics, V Holešovičkách 2, 180 00 Prague 8, Czech Republic NASA Goddard Space Flight Center, Code 673, 8800 Greenbelt Road, Greenbelt, MD 20771, USA
 Received 2023 December 18; revised 2024 February 23; accepted 2024 March 2; published 2024 April 10

Abstract

We study solar wind turbulence anisotropy in the inertial and energy-containing ranges in the inbound and outbound directions during encounters 1–9 by the Parker Solar Probe (PSP) for distances between \sim 21 and 65 R_{\odot} . Using the Adhikari et al. approach, we derive theoretical equations to calculate the ratio between the 2D and slab fluctuating magnetic energy, fluctuating kinetic energy, and the outward/inward Elsässer energy in the inertial range. For this, in the energy-containing range, we assume a wavenumber k^{-1} power law. In the inertial range, for the magnetic field fluctuations and the outward/inward Elsässer energy, we consider that (i) both 2D and slab fluctuations follow a power law of $k^{-5/3}$, and (ii) the 2D and slab fluctuations follow the power laws with $k^{-5/3}$ and $k^{-3/2}$, respectively. For the velocity fluctuations, we assume that both the 2D and slab components follow a $k^{-3/2}$ power law. We compare the theoretical results of the variance anisotropy in the inertial range with the derived observational values measured by PSP, and find that the energy density of 2D fluctuations is larger than that of the slab fluctuations. The theoretical variance anisotropy in the inertial range relating to the $k^{-5/3}$ and $k^{-3/2}$ power laws between 2D and slab turbulence exhibits a smaller value in comparison to assuming the same power law $k^{-5/3}$ between 2D and slab turbulence. Finally, the observed turbulence energy measured by PSP in the energy-containing range is found to be similar to the theoretical result of a nearly incompressible/slab turbulence description.

Unified Astronomy Thesaurus concepts: Interplanetary turbulence (830); Magnetohydrodynamics (1964); Solar wind (1534)

1. Introduction

Anisotropy is an important property of solar wind fluctuations, describing the changes in the properties of turbulence with respect to a direction relative to the magnetic field. Several characterizations, such as (i) spectral anisotropy (Horbury et al. 2008; Podesta 2009; Bruno & Telloni 2015); (ii) variance anisotropy (Bieber et al. 1996; Milano et al. 2004; Smith et al. 2006; Pine et al. 2020; Adhikari et al. 2022; Zhao et al. 2022), and (iii) correlation anisotropy (Dasso et al. 2005, 2008; Weygand et al. 2009; Wang et al. 2019; Bandyopadhyay & McComas 2021) have been used to study the anisotropy in the solar wind fluctuations. Spectral anisotropy refers to anisotropy relative to the direction of the wavevector k. By contrast, variance anisotropy refers to the magnitude of fluctuations in directions parallel and perpendicular to the mean magnetic field. As a result, these two concepts are independent of each other (Matthaeus et al. 1996; Oughton et al. 2015).

Using Parker Solar Probe (PSP) magnetometer data and following the approach used in Bieber et al. (1996), Bandyopadhyay & McComas (2021), and Zhao et al. (2022), we concluded that the energy density of 2D fluctuations relative to the slab fluctuations is smaller close to the Sun than

Original content from this work may be used under the terms of the Creative Commons Attribution 4.0 licence. Any further distribution of this work must maintain attribution to the author(s) and the title of the work, journal citation and DOI.

at larger distances. Specifically, Zhao et al. (2022) found that over the distances of 27.95–64.5 R_{\odot} , the ratio between the amplitudes of 2D and slab magnetic energies is about 0.43 (or 30%:70%), and between 64.5 and 129 R_{\odot} , it is about 1.63 (or 62%:38%). Their results differ from those observed at 1 au by Bieber et al. (1996), where the ratio between the amplitudes of 2D and slab turbulence is about 4:1. The result of Bieber et al. (1996) is similar to the theoretical prediction of a nearly incompressible magnetohydrodynamic (NI MHD) theory for a $\beta_p \sim O(1)$ or $\ll 1$ plasma beta regime (Zank & Matthaeus 1992a, 1992b, 1993; Zank et al. 2020).

In a similar study, Adhikari et al. (2022) used measurements from both PSP and Solar Orbiter (SolO) together with the $\beta_p \sim O(1)$ NI MHD turbulence model (Zank et al. 2017) to study the evolution of 2D and slab turbulence in the inner heliosphere. The geometry between the mean magnetic field and mean solar wind speed, characterized by the angle θ_{UB} (θ_{UB} is the angle between the mean solar wind speed and mean magnetic field, see Bieber et al. 1996; Zank et al. 2020), allows one to differentiate between slab and 2D fluctuations observed in the solar wind. By measuring turbulent fluctuations in parallel (0° $<\theta_{UB}<25^{\circ}$ or $155^{\circ}<\theta_{UB}<180^{\circ}$) or orthogonal $(65^{\circ} < \theta_{UB} < 115^{\circ})$ geometry, Adhikari et al. (2022) identified slab or 2D turbulence. Their results suggested that PSP primarily measures slab-like turbulence near the perihelion of the first orbit. By contrast, SolO observes both 2D and slab turbulence more frequently, with 2D turbulence energy

exceeding the slab turbulence energy. The results presented by Adhikari et al. (2022) correspond to the energy-containing range only. This manuscript investigates the evolution of anisotropic turbulence in the inertial and energy-containing ranges near the Sun in the super-Alfvénic solar wind flow in the range of \sim 21–70 R_{\odot} , from a region closer to the Sun than that studied previously by Bandyopadhyay & McComas (2021), Zhao et al. (2022), and Adhikari et al. (2022).

Zank et al. (2017) developed the NI MHD turbulence transport model equations in the $\beta_p \sim O(1)$ regime for calculating the radial evolution of 2D and slab turbulence components in the energy-containing range (see also Wang et al. 2022, for an NI MHD turbulence transport model formulation in the $\beta_p \ll 1$ regime). Adhikari et al. (2017) derived a theoretical equation for the power anisotropy of magnetic field fluctuations in the inertial range as a function of energy-containing range fluctuating magnetic energy and the correlation length. They found that for heliocentric distances of 2-10 au, the ratio between 2D and slab magnetic fluctuations in the inertial range varies between 2.5 and 5, and then gradually approaches 1 with increasing heliocentric distance. In this study, we use the Adhikari et al. (2017) approach to calculate theoretically the ratio between the inertial range 2D and slab variances for magnetic field fluctuations, velocity fluctuations, and Elsässer energies. For this, we derive the equations for the magnetic field fluctuations, the outward and inward Elsässer energies using two approaches: one in which both 2D and slab turbulence components follow a power law of $k^{-5/3}$ (where k is the magnitude of the wavenumber), and the other in which the 2D and slab components follow the power laws of $k^{-5/3}$ and $k^{-3/2}$, respectively. Similarly, we also derive the corresponding equation for the velocity fluctuations, where 2D and slab components follow a power law of $k^{-3/2}$. As the theoretical 2D and slab turbulence energies and correlation lengths in the energy-containing range are required to calculate the inertial range turbulence anisotropy, we obtain them by numerically solving the solar wind (SW) + NI MHD turbulence transport model equations (Zank et al. 2017; Adhikari et al. 2022). On the other hand, we derive the observed ratio between the 2D and slab turbulence energies in the inertial range directly from the PSP measurements, by exploiting the geometry between the background magnetic field and the solar wind speed (Bieber et al. 1996; Zank et al. 2020; Adhikari et al. 2022).

This paper is organized as follows. In Section 2, we present the theory of MHD inertial range turbulence. Section 3 discusses the observed transverse turbulence energy versus the angle between the observed mean magnetic field and the observed mean solar wind speed. Section 4 discusses the comparison between the theoretical and observed results. Finally, we summarize our work in Section 5.

2. MHD Inertial Range Turbulence Theory

The correlation tensors for slab $(P_{ij}^{sl}(\mathbf{k}))$ and 2D $(P_{ij}^{2D}(\mathbf{k}))$ turbulence are given by Zank (2014)

$$P_{ij}^{\rm sl}(\mathbf{k}) = g^{\rm sl}(k_{\parallel}) \frac{\delta(k_{\perp})}{k_{\perp}} \delta_{ij} \text{ if } i, j = x, y,$$
 (1)

and

$$P_{ij}^{\text{2D}}(\mathbf{k}) = \begin{cases} g^{\text{2D}}(k_{\perp}) \frac{\delta(k_{\parallel})}{k_{\perp}} \left[\delta_{ij} - \frac{k_i k_j}{k^2} \right], & \text{if } i, j = x, y \\ 0, & \text{if } i \text{ or } j = z, \end{cases}$$
 (2)

and $P_{i\bar{z}}^{\rm sl}=0=P_{zj}^{\rm sl}$. The functions $g^{\rm sl}(k_{||})$ and $g^{\rm 2D}(k_{\perp})$ depend on parallel and perpendicular wavevectors only. Using Equations (1) and (2), and making the assumption that the 2D and slab magnetic fluctuations follow the power laws of the form k^{-1} in the energy-containing range and $k^{-5/3}$ in the inertial range, Adhikari et al. (2017) derived the equation for the ratio of the variances between the 2D and slab magnetic fluctuations in the inertial range as

$$\frac{\langle B_{2D}^2 \rangle^{ir}}{\langle B_{sl}^2 \rangle^{ir}} = \frac{\langle B_{2D}^2 \rangle^{er}}{\langle B_{sl}^2 \rangle^{er}} \left(\frac{\lambda_{sl}^b}{\lambda_{2D}^b} \right)^{2/3}$$

$$\frac{\log (2\pi (\lambda_{sl}^b)^{-1}/k_{inj})}{\log (2\pi (\lambda_{2D}^b)^{-1}/k_{inj})},$$
(3)

where $\langle B_{\rm 2D}^2 \rangle^{\rm ir/er}$ and $\langle B_{\rm sl}^2 \rangle^{\rm ir/er}$ denote the variances of 2D and slab magnetic fluctuations in the inertial/energy-containing range, and $\lambda_{\rm 2D}^b$ and $\lambda_{\rm sl}^b$ denote the 2D and slab correlation lengths in the energy-containing range, and $k_{\rm inj} \sim 1.07 \times 10^{-9} \, {\rm km}^{-1}$ (Adhikari et al. 2017) is the injection wavenumber. We assume $k = 2\pi/\lambda$, where λ is the correlation length.

Following the methodology of Adhikari et al. (2017) and assuming that the 2D and slab outward and inward Elsässer energies exhibit power laws of k^{-1} and $k^{-5/3}$ in the energy-containing and inertial ranges, the ratio between the 2D and slab variances of the outward/inward Elsässer energies in the inertial range can be expressed as

$$\frac{\langle z_{2D}^{+2} \rangle^{ir}}{\langle z_{sl}^{+2} \rangle^{ir}} = \frac{\langle z_{2D}^{+2} \rangle^{er}}{\langle z_{sl}^{+2} \rangle^{er}} \left(\frac{\lambda_{sl}^{+}}{\lambda_{2D}^{+}} \right)^{2/3}
\frac{\log (2\pi (\lambda_{sl}^{+})^{-1} / k_{inj})}{\log (2\pi (\lambda_{2D}^{+})^{-1} / k_{inj})};$$
(4)

$$\frac{\langle z_{\text{2D}}^{-2} \rangle^{\text{ir}}}{\langle z_{\text{sl}}^{-2} \rangle^{\text{ir}}} = \frac{\langle z_{\text{2D}}^{-2} \rangle^{\text{er}}}{\langle z_{\text{sl}}^{-2} \rangle^{\text{er}}} \left(\frac{\lambda_{\text{sl}}^{-}}{\lambda_{\text{2D}}^{-2}} \right)^{2/3}$$

$$\frac{\log (2\pi (\lambda_{\text{sl}}^{-})^{-1} / k_{\text{inj}})}{\log (2\pi (\lambda_{\text{2D}}^{-})^{-1} / k_{\text{inj}})}, \tag{5}$$

where $\langle z_{2D}^{\pm 2} \rangle^{\rm ir/er}$ and $\langle z_{\rm sl}^{\pm 2} \rangle^{\rm ir/er}$ denote the 2D and slab outward/inward Elsässer energies in the inertial/energy-containing range, and $\lambda_{\rm 2D}^{\pm}$ and $\lambda_{\rm sl}^{\pm}$ denote the corresponding 2D and slab correlation lengths in the energy-containing range. We note that Equations (3)–(5) are derived assuming the same power-law form of $k^{-5/3}$ for 2D and slab fluctuating magnetic energy and Elsässer energies. It has been found that the observed magnetic fluctuations (Chen et al. 2020) and Elsässer energies (Zank et al. 2022) exhibit a $k^{-3/2}$ power law near the Sun. If 2D and slab magnetic field fluctuations, and outward and inward Elsässer energies follow the power laws of $k^{-5/3}$ and $k^{-3/2}$, respectively, the ratios between 2D and slab components in the

inertial range take the following form:

$$\frac{\langle B_{2D}^2 \rangle^{ir}}{\langle B_{sl}^2 \rangle^{ir}} = \frac{3}{4} \frac{\langle B_{2D}^2 \rangle^{er}}{\langle B_{sl}^2 \rangle^{er}} \frac{(\lambda_{sl}^b)^{1/2}}{(\lambda_{2D}^b)^{2/3}} \frac{\log (2\pi (\lambda_{sl}^b)^{-1}/k_{inj})}{\log (2\pi (\lambda_{2D}^b)^{-1}/k_{inj})}$$

$$\left(\frac{U}{2\pi f_1}\right)^{1/6} \frac{1 - (f_1/f_2)^{2/3}}{1 - (f_1/f_2)^{1/2}}; \tag{6}$$

$$\frac{\langle z_{\rm 2D}^{+2} \rangle^{\rm ir}}{\langle z_{\rm sl}^{+2} \rangle^{\rm ir}} = \frac{3}{4} \frac{\langle z_{\rm 2D}^{+2} \rangle^{\rm er}}{\langle z_{\rm sl}^{+2} \rangle^{\rm er}} \frac{(\lambda_{\rm sl}^+)^{1/2}}{(\lambda_{\rm 2D}^+)^{2/3}} \frac{\log{(2\pi(\lambda_{\rm sl}^+)^{-1}/k_{\rm inj})}}{\log{(2\pi(\lambda_{\rm 2D}^+)^{-1}/k_{\rm inj})}}$$

$$\left(\frac{U}{2\pi f_1}\right)^{1/6} \frac{1 - (f_1/f_2)^{2/3}}{1 - (f_1/f_2)^{1/2}};$$
(7)

$$\frac{\langle z_{\rm 2D}^{-2} \rangle^{\rm ir}}{\langle z_{\rm sl}^{-2} \rangle^{\rm ir}} = \frac{3}{4} \frac{\langle z_{\rm 2D}^{-2} \rangle^{\rm er}}{\langle z_{\rm sl}^{-2} \rangle^{\rm er}} \frac{(\lambda_{\rm sl}^{-})^{1/2}}{(\lambda_{\rm 2D}^{-})^{2/3}} \frac{\log{(2\pi(\lambda_{\rm sl}^{-})^{-1}/k_{\rm inj})}}{\log{(2\pi(\lambda_{\rm 2D}^{-})^{-1}/k_{\rm inj})}}$$

$$\left(\frac{U}{2\pi f_1}\right)^{1/6} \frac{1 - (f_1/f_2)^{2/3}}{1 - (f_1/f_2)^{1/2}},\tag{8}$$

where f_1 and f_2 are the frequencies in the inertial range, and $f_2 > f_1$. We use the relation $\omega = 2\pi f = kU \Rightarrow k = 2\pi f/U$, where $(\omega)f$ is the (angular) frequency, and U is the solar wind speed to convert a wavenumber into a frequency provided the solar wind flow is super-Alfvénic. Here, we use $f_1 = 1.7 \times 10^{-3}$ and $f_2 = 1.7 \times 10^{-2}$ Hz, corresponding to a 10 minute long interval data set with a resolution of 1 minute, and excluding the kinetic effects. We note that Equations (6)–(8) may not be applicable in the sub-Alfvénic solar wind flow because one may need to use a modified Taylor hypothesis to convert a wavenumber into a frequency (see Zank et al. 2022).

To derive the ratio between the 2D and slab variances of solar wind velocity fluctuations in the inertial range, we assume that the 2D and slab velocity fluctuations exhibit a power law of $k^{-3/2}$ in the inertial range. Note that the assumption of a $k^{-3/2}$ power law is not related to that of magnetic field fluctuations or Elsässer energies. This is based on observational studies (e.g., Zhao et al. 2020; Kasper et al. 2021) that often find that solar wind velocity fluctuations follow a power law of $k^{-3/2}$. The expression for the ratio between the 2D and slab velocity fluctuating energies in the inertial range can be expressed as

$$\frac{\langle u_{2D}^2 \rangle^{ir}}{\langle u_{sl}^2 \rangle^{ir}} = \frac{\langle u_{2D}^2 \rangle^{er}}{\langle u_{sl}^2 \rangle^{er}} \left(\frac{\lambda_{sl}^u}{\lambda_{2D}^u} \right)^{1/2}
\frac{\log (2\pi (\lambda_{sl}^u)^{-1}/k_{inj})}{\log (2\pi (\lambda_{2D}^u)^{-1}/k_{inj})},$$
(9)

where $\langle u_{\rm 2D}^2 \rangle^{\rm ir/er}$ and $\langle u_{\rm si}^2 \rangle^{\rm ir/er}$ denote the 2D and slab velocity fluctuations in the inertial/energy-containing range, and $\lambda_{\rm 2D}^u$ and $\lambda_{\rm sl}^u$ denote the 2D and slab correlation lengths of the velocity fluctuations in the energy-containing range. Equations (3)–(9) contain the energy-containing range 2D and NI/slab turbulence energies and correlation lengths, which are obtained by numerically solving the SW + NI MHD turbulence transport model equations (Adhikari et al. 2022). In this study, Equations (3)–(9) provide the theoretical result of the ratio between the 2D and slab turbulence energies in the inertial range, which are then compared against PSP measurements from encounters 1–9.

3. Turbulence Energy versus θ_{UB}

In Figure 1, we show two different results obtained from a day-long data set at the same heliocentric distance of \sim 0.18 au during the PSP E9 encounter on 2021 August 6 (in the inbound direction). The result shown in blue is calculated using 10 minute long intervals, which represents the inertial range. The result shown in magenta is calculated using 4 hr long intervals, representing the energy-containing range. In Figure 1(A), we plot a histogram of θ_{UB} . The blue histogram ranges from 90°–70°, and exhibits a negative skewness of -1.47. Similarly, the magenta histogram ranges from 155°–175°, and shows a negative skewness of -0.78.

Using a day-long data set from 2021 August 6, we first compute the transverse turbulence energies using 10 minute and 4 hr long intervals, thereby eliminating the compressible longitudinal (parallel to the mean magnetic field **B**) components (Belcher & Davis 1971; Adhikari et al. 2022). We then smooth the observed transverse components by binning the results with a bin width of 10° (Figures 1(B)–(G)). It is evident from Figure 1 that the transverse fluctuating magnetic energy $\langle B_{\perp}^2 \rangle$, transverse fluctuating kinetic energy $\langle u_{\perp}^2 \rangle$, and transverse Elsässer energies $\langle z_{\perp}^{\pm 2} \rangle$ in the inertial range (represented by blue curves/stars) decrease as the angle θ_{UB} increases from $\theta_{UB} = 97^{\circ}$ to $\theta_{UB} = 165^{\circ}$. Similarly, the $\langle B_{\perp}^2 \rangle$, $\langle u_{\perp}^2 \rangle$, and $\langle z_{\perp}^{\pm 2} \rangle$ in the energy-containing range (denoted by magenta curves/ stars) show a slight decrease as θ_{UB} ranges from $160^{\circ}-169^{\circ}$. Based on the assumption that turbulence measured in a highly oblique flow $\theta_{UB} \rightarrow [65^{\circ}-115^{\circ}]$ or in a highly field-aligned flow $\theta_{UB} \rightarrow [0^{\circ}-25^{\circ}]$ or $[155^{\circ}-180^{\circ}]$ can be regarded as 2D or slab turbulence, respectively (Bieber et al. 1996; Zank et al. 2020; Adhikari et al. 2022), Figure 1 shows that the inertial range turbulence consists of both 2D and slab turbulence, whereas the energy-containing range turbulence consists of slab turbulence only. However, PSP may also observe the energy-containing range of 2D turbulence near the Sun, although it is not very large (see Table 1). Note that the result shown in Figure 1 is based on the geometry between the mean solar wind speed and the mean magnetic field over 10 minute and 4 hr long intervals. During a 4 hr long interval, the average of the background magnetic field and solar wind speed effectively eliminates 2D turbulence. Whereas during a 10 minute long interval, most background fields are arranged radially. However, there are also cases where the background fields are highly oblique (see Figure 1(A) and Table 1).

Based on the observed inertial range results (blue stars) shown in Figures 1(B)–(G), we derive the ratio between the 2D and slab turbulence energy. Here, the inertial range 2D component is determined from the transverse component satisfying the criterion $65^{\circ} < \theta_{UB} < 115^{\circ}$, and taking averaged values. Similarly, the inertial range slab component is determined from the transverse component satisfying the criterion $\theta_{UB} \rightarrow [0^{\circ}-25^{\circ}]$ or $[155^{\circ}-180^{\circ}]$, and taking the averaged values. In so doing, we assume that the solar wind plasma properties are similar within the ~ 1 day period. The ratio between the inertial range 2D and slab turbulence components is as follows: (i) turbulent magnetic energy shows a ratio of 2.9 (Figure 1(B)), (ii) turbulent kinetic energy shows a ratio of 1.34 (Figure 1(C)), (iii) outward Elsässer energy shows a ratio of 3.18 (Figure 1(D)), and (iv) inward Elsässer energy shows a ratio of 10.92 (Figure 1(E)). In contrast to the results of Bandyopadhyay & McComas (2021) and Zhao et al. (2022), the 2D turbulence energy exceeds the slab turbulence

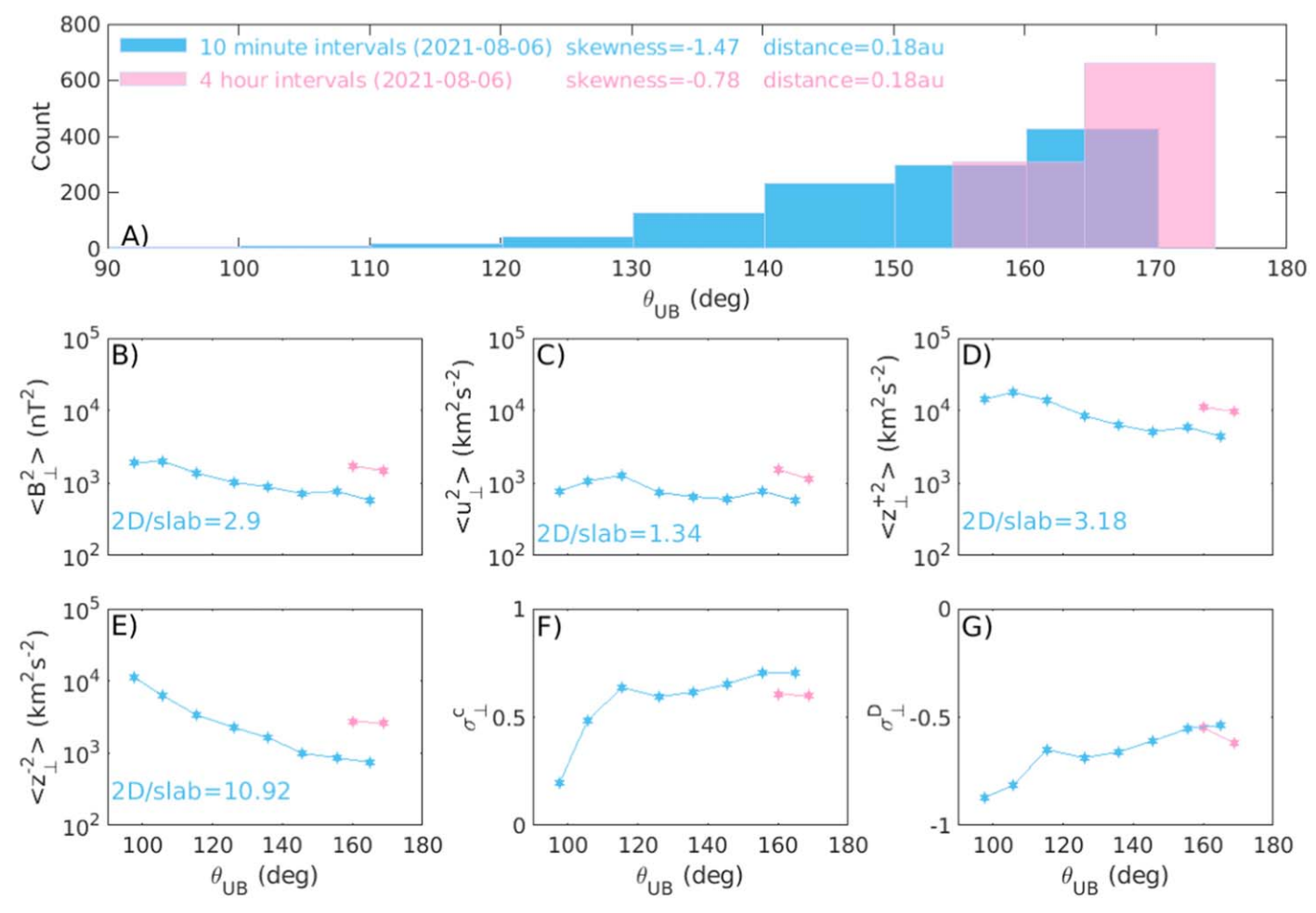


Figure 1. Panel (A): histogram of the angle between the mean solar wind speed and the mean magnetic field (θ_{UB}) corresponding to 10 minute and 4 hr long intervals measured by PSP at 0.18 au during E9 on 2021 August 6 (in the inbound direction). Panels (B)–(G) represent the transverse fluctuating magnetic energy, fluctuating kinetic energy, outward Elsässer energy, inward Elsässer energy, normalized cross helicity, and normalized residual energy as a function of θ_{UB} , respectively. These quantities are calculated by binning the results with a 10° bin width. The results in blue and magenta are calculated in 10 minute and a 4 hr long intervals, respectively.

Table 1 Values of θ_{UB} Computed during 4 hr and 10 minute Long Intervals in Both the Inbound and Outbound Directions from Encounters 1–9 of PSP between \sim 21 and 65 R_{\odot}

	Inbou	nd Direction	Outbound Direction		
θ_{UB} values Fall within the range	4 hr long interval Total No.	10 minute long interval Total No.	4 hr Long Interval Total No.	10 minute long interval Total No.	
[0°-180°]	274 (100%)	3843 (100%)	184 (100%)	3840 (100%)	
[65°–115°]	21 (7.66%)	396 (10.3%)	15 (8.15%)	453 (11.79%)	
$[0^{\circ}-25^{\circ}]$ or $[155^{\circ}-180^{\circ}]$	160 (58.39%)	1660 (43.19%)	101 (54.89%)	1627 (42.23%)	

energy in accordance with the NI MHD turbulence theory in the low and O(1) plasma beta regimes (Zank & Matthaeus 1992b, 1993; Zank et al. 2017).

The inertial range normalized cross helicity (blue stars/curve) σ_{\perp}^c , which measures the energy difference between the outward and inward Elsässer energies, shows a value of \sim 0.7 at $\theta_{UB} = 165^{\circ}$ and \sim 0.2 at $\theta_{UB} = 97^{\circ}$ (Figure 1(F)), meaning that the σ_{\perp}^c is larger in the field-aligned flow than in the orthogonal flow. Similarly, the inertial range normalized residual energy (blue stars/curve) σ_{\perp}^D , which measures the energy difference between the fluctuating kinetic energy and magnetic energy density, is about -0.5 at $\theta_{UB} = 165^{\circ}$ and about -0.9 at $\theta_{UB} = 97^{\circ}$ (Figure 1(G)), indicating that in the highly oblique

flow, the solar wind fluctuations are more dominated by fluctuating magnetic energy compared to field-aligned flows.

4. Radial Evolution of Anisotropic Turbulence

In this section, we discuss the radial evolution of 2D and slab turbulence energies theoretically and observationally as a function of heliocentric distance in the inbound and outbound directions. We select the PSP SWEAP/SPAN, and FIELDS data sets from encounters 1–9 (Bale et al. 2016; Kasper et al. 2016), and divide the data into inbound and outbound directions. We discard data with wind speeds larger than $450 \, \mathrm{km \, s^{-1}}$. In both directions, we first compute the transverse turbulence energies $(\langle B_L^2 \rangle, \langle u_L^2 \rangle, \mathrm{and} \langle z_L^{\pm 2} \rangle)$, and the angle θ_{UB} in

Table 2

Radial Profiles of the Observed Transverse Fluctuating Magnetic Energy, Transverse Fluctuating Kinetic Energy, Transverse Outward/Inward Elsässer Energy, and the Transverse Normalized Cross Helicity in the Inbound and Outbound Directions during Encounters 1–9 of PSP between ${\sim}21$ and 65 R_{\odot}

Energy-containing Range		
Turbulence	Inbound Direction	Outbound Direction
$\langle B_{\perp}^2 \rangle$	$r^{-3.6\pm0.18}$	$r^{-3.85\pm0.27}$
$\langle u_{\perp}^2 \rangle$	$r^{-0.94\pm0.19}$	$r^{-2.79\pm0.63}$
$\langle z_{\perp}^{+2} \rangle$	$r^{-0.99\pm0.22}$	$r^{-1.99\pm0.46}$
$\langle z_{\perp}^{-2} \rangle$	$r^{-0.44\pm0.38}$	$r^{-0.76\pm0.26}$
σ^c_{\perp}	$r^{-0.44\pm0.06}$	$r^{-0.5\pm0.22}$

the 4 hr and 10 minute long intervals. In Table 1, we show the θ_{UB} values computed during 4 hr and 10 minute long intervals for the inbound and outbound directions in the super-Alfvénic solar wind flow between \sim 21 and 80 R_{\odot} . In the inbound and outbound directions, the total number of θ_{UB} values calculated over 4 hr long intervals that fall within the [65°-115°] range are 21 and 15, respectively. Meanwhile, the number of $\theta_{I/R}$ values that fall within the $[0^{\circ}-25^{\circ}]$ or $[155^{\circ}-180^{\circ}]$ range are 160 and 101, respectively. As there are only a limited number (21 and 15) of θ_{UB} values in the $[65^{\circ}-115^{\circ}]$ range, these data points are excluded to prevent statistical inadequacies. Similarly, for 10 minute long intervals, the total number of θ_{UB} values within the [65°-115°] range are 396 and 453 for the inbound and outbound directions, respectively, and those within the [0°-25°] or [155°-180°] range are 1660 and 1627, respectively. Notably, the number of θ_{UB} values derived from 4 hr long intervals is lower than those from 10 minute long intervals. Averaging the background fields using 4 hr long intervals can reduce nonradial flow and make it more radially aligned. To determine the radial evolution of turbulence energy in the inbound and outbound directions, we calculate the mean value of the energy-containing range transverse turbulence energies over a bin width of 10.75 R_{\odot} . The radial profiles of the observed energy-containing range $\langle B_{\perp}^2 \rangle$, $\langle u_{\perp}^2 \rangle$, $\langle z_{\perp}^{\pm 2} \rangle$, and σ_{\perp}^c in the inbound and outbound directions are shown in Table 2. Applying the above previously discussed criteria for θ_{UB} over a bin width of 10.75 R_{\odot} , we derive the 2D and slab turbulence energies from the observed inertial range transverse turbulence energies, and the ratio between them. Table 3 shows the radial profiles of the ratio between the observed inertial range 2D and slab fluctuating magnetic energy, fluctuating kinetic energy, outward Elsässer energy, and inward Elsässer energy in the inbound and outbound directions. We use these observed results to validate the model results obtained from the theory discussed in Section 2.

First, we solve the SW + NI MHD turbulence transport model equations (Adhikari et al. 2022) with specific boundary conditions (BCs) for both inbound and outbound directions, as shown in Table 4. The BCs for slab turbulence and solar wind parameters are obtained from the PSP measurements. For 2D turbulence, the BCs are derived by scaling the BCs for slab turbulence. In the inbound direction, the BCs for 2D turbulence energy and 2D correlation length are assumed to be 3.5 and 0.5 times those for slab turbulence. By contrast, in the outbound direction, the BCs for 2D turbulence energy and 2D correlation length are assumed to be 2.5 and 0.5 times those for slab turbulence. We use different multiplicative factors in the inbound and outbound directions because the variance

Table 3

Radial Profiles of the Ratio between the Observed Inertial Range 2D and Slab Turbulence Energies in the Inbound and Outbound Directions during Encounters 1–9 of PSP for Distances between \sim 21 and 65 R_{\odot}

Inertial Range Turbulence	Inbound Direction	Outbound Direction
$\langle B_{\rm 2D}^2 \rangle / \langle B_{\rm sl}^2 \rangle$	$r^{-0.37\pm0.49}$ $r^{-0.44\pm0.42}$	r ^{0.05±0.19}
$\langle u_{\rm 2D}^2 \rangle / \langle u_{\rm sl}^2 \rangle$ $\langle z_{\rm 2D}^{+2} \rangle / \langle z_{\rm sl}^{+2} \rangle$	$r^{-0.38\pm0.57}$	$r^{0.76\pm0.12}$ $r^{0.94\pm0.12}$
$\langle z_{\rm 2D}^{-2} \rangle / \langle z_{\rm sl}^{-2} \rangle$	$r^{0.22\pm0.57}$	$r^{0.34\pm0.26}$

anisotropy becomes different in these two directions. Table 5 shows the parameter values used in the SW + NI MHD turbulence model for the inbound and outbound directions. We compare the theoretical results of the energy-containing range turbulence energies with the observed results measured by PSP. Then, we calculate the theoretical results of the ratio between the inertial range 2D and slab turbulence components as a function of distance, and compare them with the PSP measurements.

4.1. Inbound Direction

We first discuss the evolution of the energy-containing range 2D and slab turbulence energies with distance. As shown in Figure 2, we compare the theoretical and observed slab fluctuating magnetic energy (Figure 2(A)), slab fluctuating kinetic energy (Figure 2(B)), slab outward Elsässer energy (Figure 2(C)), slab inward Elsässer energy (Figure 2(D)), slab normalized cross helicity (Figure 2(E)), and slab normalized residual energy (Figure 2(F)) with increasing distance. In the figure, the solid orange curve corresponds to the theoretical NI/ slab turbulence prediction, the solid yellow curve to the theoretical 2D turbulence, and the blue stars/dotted curve identifies the observed slab turbulence quantities. Notably, both the observed slab magnetic energy and the theoretical NI/slab magnetic energy are relatively close with increasing distance. Nevertheless, the observed slab turbulent energy experiences a more rapid decrease compared to the theoretical NI/slab result. The theoretical and observed slab magnetic energy stays below the theoretical 2D magnetic energy. Regarding the turbulent kinetic energy, the theoretical NI/slab kinetic energy aligns reasonably closely with the observed kinetic energy. Furthermore, the theoretical 2D $\langle u^2 \rangle$ decreases more rapidly compared to the theoretical NI/slab $\langle u^2 \rangle$.

As distance increases, both the theoretical 2D and NI/slab $\langle z^{+2} \rangle$ decrease. Similarly, the observed $\langle z^{+2} \rangle$ also decreases, and is relatively close to the theoretical NI/slab $\langle z^{+2} \rangle$. The observed $\langle z^{-2} \rangle$ decreases with increasing distance, closely aligning with the theoretical NI/slab $\langle z^{-2} \rangle$. The theoretical $\langle z^{\infty-2} \rangle$ shows a decrease with distance.

The theoretical NI/slab normalized cross helicity and normalized residual energy show a decreasing radial profile with increasing distance, which are similar to the corresponding observed values. Furthermore, the theoretical 2D normalized cross helicity and 2D normalized residual energy decrease more rapidly than their NI/slab counterparts.

Figure 3(A) shows a comparison between the theoretical and observed results of the ratio between inertial range 2D and slab fluctuating magnetic energy, $\langle B_{\rm 2D}^2 \rangle^{\rm ir}/\langle B_{\rm sl}^2 \rangle^{\rm ir}$, and $\langle B_{\rm 2D}^2 \rangle^{\rm 10MIN}/\langle B_{\rm sl}^2 \rangle^{\rm 10MIN}$, respectively, as a function of distance. In the figure, the solid orange curve is obtained assuming the

Table 4
Boundary Values of Solar Wind Parameters and Turbulence Quantities at 22.37 R_{\odot} for the Inbound Direction and at 21.55 R_{\odot} for the Outbound Direction

	Inbound Direction				Outbound Direction		
Parameters	Values	Parameters	Values	Parameters	Values	Parameters	Values
$\langle z^{\infty+2} \rangle \text{ (km}^2 \text{ s}^{-2})$	3.33×10^{4}	$\langle z^{*+2} \rangle$ (km ² s ⁻²)	9.53×10^{3}	$\langle z^{\infty+2} \rangle \text{ (km}^2 \text{ s}^{-2})$	2.31×10^{4}	$\langle z^{*+2} \rangle \text{ (km}^2 \text{ s}^{-2})$	9.23×10^{3}
$\langle z^{\infty-2} \rangle \text{ (km}^2 \text{ s}^{-2})$	4.66×10^{3}	$\langle z^{*-2} \rangle \text{ (km}^2 \text{ s}^{-2})$	1.33×10^3	$\langle z^{\infty-2} \rangle \text{ (km}^2 \text{ s}^{-2})$	2.8×10^{3}	$\langle z^{*-2} \rangle \text{ (km}^2 \text{ s}^{-2})$	1.1×10^{3}
$E_D^{\infty} (\mathrm{km}^2 \mathrm{s}^{-2})$	-3.15×10^{3}	$E_D^* (\mathrm{km}^2 \mathrm{s}^{-2})$	-9×10^{2}	$E_D^{\infty} (\mathrm{km}^2 \mathrm{s}^{-2})$	-2.5×10^{3}	$E_D^* (\mathrm{km}^2 \mathrm{s}^{-2})$	-1.0×10^{3}
λ_{∞}^{+} (km)	1.15×10^{5}	λ_*^+ (km)	2.31×10^{5}	λ_{∞}^{+} (km)	6.9×10^4	λ_*^+ (km)	1.38×10^{5}
λ_{∞}^{-} (km)	1.5×10^{5}	λ_*^- (km)	3.0×10^{5}	λ_{∞}^{-} (km)	9.65×10^4	λ_*^- (km)	1.93×10^{5}
λ_D^{∞} (km)	2.86×10^{5}	λ_D^* (km)	5.71×10^{5}	λ_D^{∞} (km)	1.70×10^{5}	λ_D^* (km)	3.4×10^{5}
T_p (K)	4.94×10^{5}	T_e (K)	3.92×10^{5}	$T_p(\mathbf{K})$	4.38×10^{5}	T_e (K)	3.5×10^{5}
$U (\mathrm{km \ s}^{-1})$	2.65×10^{2}	$\rho \ (\mathrm{cm}^{-3})$	1.36×10^{3}	$U (\mathrm{km \ s^{-1}})$	2.47×10^{2}	$\rho (\mathrm{cm}^{-3})$	1.59×10^{3}

 ${\bf Table~5}$ Values of the Parameters Used for the SW + NI MHD Turbulence Model in the Inbound and Outbound Directions

	Inbound Direction				Outbound Direction		
Parameters	Values	Parameters	Values	Parameters	Values	Parameters	Values
$V_{A0} ({\rm km \ s}^{-1})$	129.17	C_{sh}^+	0.6	$V_{A0} ({\rm km \ s}^{-1})$	97.85	C_{sh}^+	0.6
$\Delta U ({\rm km \ s}^{-1})$	200	C_{sh}^-	0.6	$\Delta U ({\rm km \ s^{-1}})$	200	C_{sh}^-	0.6
α	0.03	$C_{sh}^{E_D}$	-0.1	α	0.03	$C_{sh}^{E_D}$	-0.1
β	0.015	C_{sh}^{*+}	0.18	β	0.015	C_{sh}^{*+}	0.18
b	0.5	C_{sh}^{*-}	0.18	b	0.5	C_{sh}^{*-}	0.18
	•••	$C_{sh}^*E_D$	-0.03			$C_{sh}^*E_D$	-0.03

same $k^{-5/3}$ power law between 2D and slab turbulence. By contrast, the solid yellow curve is obtained by supposing that 2D and slab turbulence follow the power laws of $k^{-5/3}$ and $k^{-3/2}$, respectively. Clearly, the variance anisotropy of magnetic field fluctuations in the former case exceeds that in the latter case, due to the more rapid decrease of slab turbulence in the former case compared to the latter. Both the theoretical $\langle B_{2D}^2 \rangle^{\rm ir}/\langle B_{\rm sl}^2 \rangle^{\rm ir}$ and observed $\langle B_{2D}^2 \rangle^{10 \rm MIN}/\langle B_{\rm sl}^2 \rangle^{10 \rm MIN}$ results (blue stars/dotted curve) are in good agreement, with both ratios exceeding 1 between 22.37 and 70 R_{\odot} . This indicates that turbulent magnetic energy is predominantly 2D rather than slab, an interpretation more closely aligned with the NI MHD theory (Zank & Matthaeus 1992b, 1993; Zank et al. 2017).

For the fluctuating kinetic energy, the theoretical $\langle u_{\rm 2D}^2 \rangle^{\rm ir}/\langle u_{\rm sl}^2 \rangle^{\rm ir}$ decreases more rapidly within $\sim\!33~R_\odot$, followed by a slower decrease (Figure 3(B)). The theoretical ratio closely resembles the observed $\langle u_{\rm 2D}^2 \rangle^{\rm 10MIN}/\langle u_{\rm sl}^2 \rangle^{\rm 10MIN}$.

Figure 3(C) compares the theoretical $\langle z_{2D}^{+2} \rangle^{\rm ir}/\langle z_{\rm sl}^{+2} \rangle^{\rm ir}$ and the observed $\langle z_{2D}^{+2} \rangle^{\rm 10MIN}/\langle z_{\rm sl}^{+2} \rangle^{\rm 10MIN}$ with increasing distance. As before, the solid orange curve shows the theoretical result assuming the same power law of $k^{-5/3}$ for 2D and slab turbulence. Evidently, the solid orange curve exhibits a larger value in comparison to the solid yellow curve, which is calculated by assuming $k^{-5/3}$ and $k^{-3/2}$ power laws for 2D and slab turbulence, respectively. Both theoretical (solid curves) and observed (blue star symbols/dotted curves) ratios are found to be larger than 1, implying that in the inertial range $\langle z_{2D}^{+2} \rangle$ is the dominant component, and $\langle z_{\rm sl}^{+2} \rangle$ is the minority component. Likewise, Figure 3(D) compares the theoretical $\langle z_{2D}^{-2} \rangle^{\rm ir}/\langle z_{\rm sl}^{-2} \rangle^{\rm ir}$ and the observed $\langle z_{2D}^{-2} \rangle^{\rm 10MIN}/\langle z_{\rm sl}^{-2} \rangle^{\rm 10MIN}$ ratios. In this case, the solid orange curve also shows a larger value compared to the solid yellow curve. Both theoretical (solid curves) and observed (blue star symbols/dotted curves) ratios are also found to be larger than 1, indicating that the 2D

component dominates. Again, these results can be interpreted in terms of the NI MHD theory (Zank & Matthaeus 1992b, 1993; Zank et al. 2017).

4.2. Outbound Direction

Figures 2 and 4 illustrate the radial evolution of the energycontaining range 2D and slab fluctuating magnetic energy (Figure 4(A)), fluctuating kinetic energy (Figure 4(B)), outward Elsässer energy (Figure 4(C)), inward Elsässer energy (Figure 4(D)), normalized cross helicity (Figure 4(E)), and normalized residual energy (Figure 4(F)), but now for the outbound direction. The solid orange and yellow curves denote the theoretical slab and 2D turbulence energies, respectively, and the blue stars/dotted curves indicate the observed values. Clearly, Figure 4 shows that the theoretical NI/slab fluctuating magnetic energy, fluctuating kinetic energy, outward/inward Elsässer energy, normalized cross helicity, and normalized residual energy are in agreement with the corresponding observed values as a function of distance. The theoretical 2D fluctuating magnetic energy, and 2D outward/inward Elsässer energy exhibit larger values compared to their theoretical NI/ slab counterparts. However, the theoretical 2D fluctuating kinetic energy remains below the theoretical NI/slab $\langle u^2 \rangle$. Similar to the inbound direction, the theoretical 2D σ_c and σ_D in the outbound direction decrease more rapidly than the theoretical NI/slab σ_c and σ_D , respectively.

In Figure 5(A), we compare the theoretical $\langle B_{2D}^2 \rangle^{\rm ir}/\langle B_{\rm sl}^2 \rangle^{\rm ir}$ and the observed $\langle B_{2D}^2 \rangle^{\rm 10MIN}/\langle B_{\rm sl}^2 \rangle^{\rm 10MIN}$ with increasing distance, where both theoretical (solid curves) and observed (blue stars/dotted curves) results reasonably agree with each other, and exhibit values larger than 1. Similar to above, the theoretical result of $\langle B_{2D}^2 \rangle^{\rm ir}/\langle B_{\rm sl}^2 \rangle^{\rm ir}$ (solid yellow curve) assumes the same $k^{-5/3}$ power law for 2D and slab turbulence is larger than the theoretical $\langle B_{2D}^2 \rangle^{\rm ir}/\langle B_{\rm sl}^2 \rangle^{\rm ir}$ (solid yellow curve) obtained by

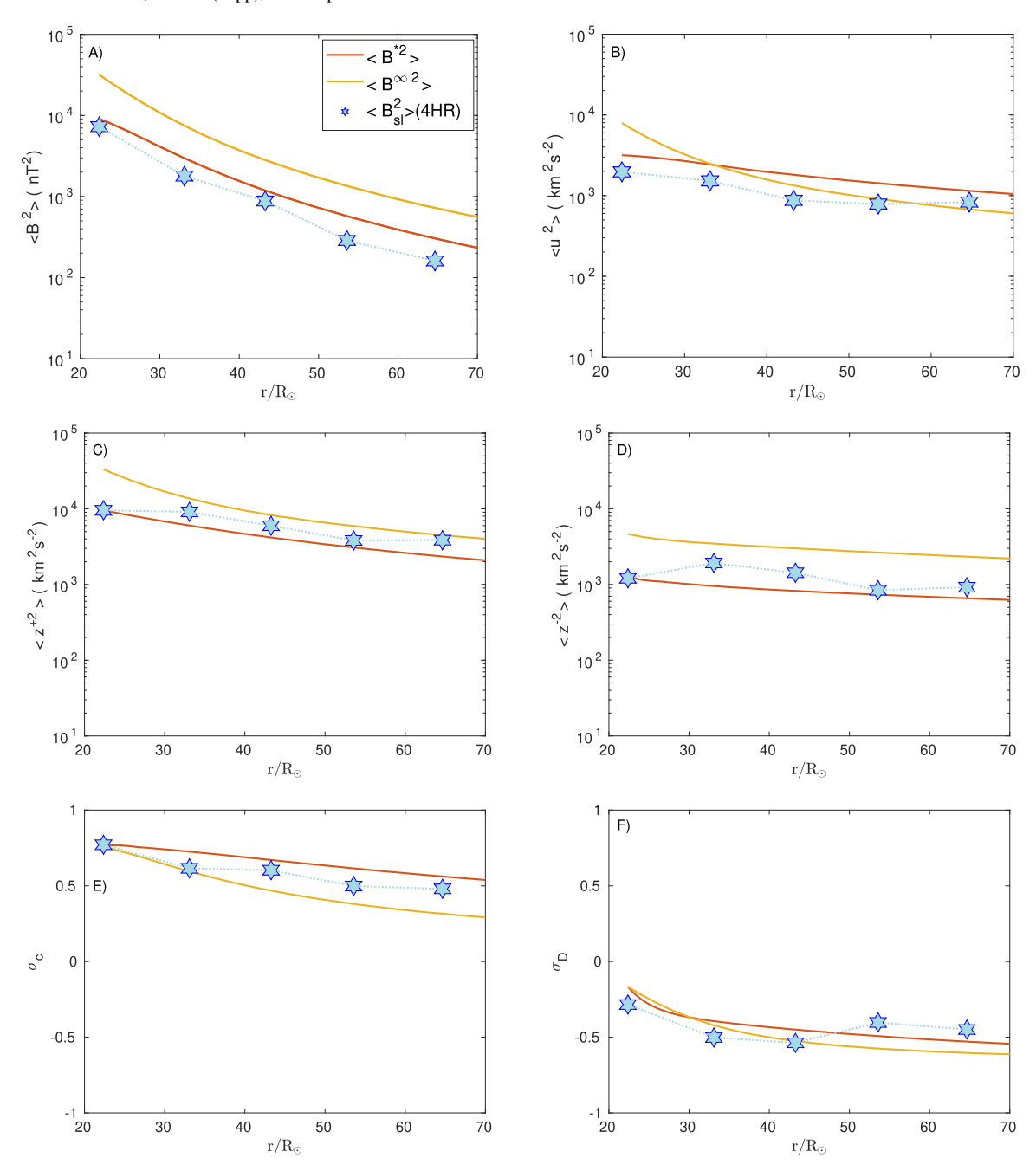


Figure 2. Comparison between the theoretical and observed energy-containing range 2D and slab fluctuating magnetic energy (A), fluctuating kinetic energy (B), outward Elsässer energy (C), inward Elsässer energy (D), normalized cross helicity (E), and normalized residual energy (F) as a function of distance in the inbound direction during encounters 1–9 of PSP. Blue stars/dotted curves denote the observed slab turbulence energy calculated using 4 hr long intervals. Solid yellow curves represent the theoretical NI/slab results, and the solid orange curves the theoretical 2D results.

assuming $k^{-5/3}$ and $k^{-3/2}$ power laws for 2D and slab turbulence, respectively. We find again that the inertial range 2D fluctuating magnetic energy dominates the inertial range slab fluctuating magnetic energy. In Figure 5(B), the average observed $\langle u_{\rm 2D}^2 \rangle^{\rm 10MIN} / \langle u_{\rm sl}^2 \rangle^{\rm 10MIN}$ is less than 1 from 22.56 to 41.65 R_{\odot} , and then increases, while the theoretical $\langle u_{\rm 2D}^2 \rangle^{\rm ir} / \langle u_{\rm sl}^2 \rangle^{\rm ir}$ decreases from 22.56 to 41.65 R_{\odot} , and then remains approximately constant.

Figure 5(C) compares the theoretical $\langle z_{2\mathrm{D}}^{+2} \rangle^{\mathrm{ir}} / \langle z_{\mathrm{sl}}^{+2} \rangle^{\mathrm{ir}}$ and the observed $\langle z_{2\mathrm{D}}^{+2} \rangle^{10\mathrm{MIN}} / \langle z_{\mathrm{sl}}^{+2} \rangle^{10\mathrm{MIN}}$ as a function of heliocentric distance. The theoretical (solid curves) and observed (blue stars/dotted curves) results show reasonable agreement, with the theoretical inertial range $\langle z_{2\mathrm{D}}^{+2} \rangle$ consistently larger than the

theoretical inertial range $\langle z_{\rm sl}^{+2} \rangle$, but the observed ratio is less than 1 within 41.65 R_{\odot} , and then larger than 1. Here, the solid orange curve (for a $k^{-5/3}$ power law for both 2D and slab turbulence) also shows a larger value compared to the solid yellow curve (assuming a $k^{-5/3}$ power law for 2D turbulence and a $k^{-3/2}$ power law for slab turbulence) as a function of distance. Similarly, in Figure 5(D), the theoretical $\langle z_{\rm 2D}^{-2} \rangle^{\rm ir} / \langle z_{\rm sl}^{-2} \rangle^{\rm ir}$ (solid yellow curve) is consistent with the observed $\langle z_{\rm 2D}^{-2} \rangle^{\rm 10MIN} / \langle z_{\rm sl}^{-2} \rangle^{\rm 10MIN}$, with the theoretical and observed ratios being larger than 1. The orange curve exhibits a larger value than the yellow curve. Again, the interpretation of these results is consistent with the beta small or O(1) plasma beta NI MHD theory (Zank & Matthaeus 1992a, 1992b, 1993;

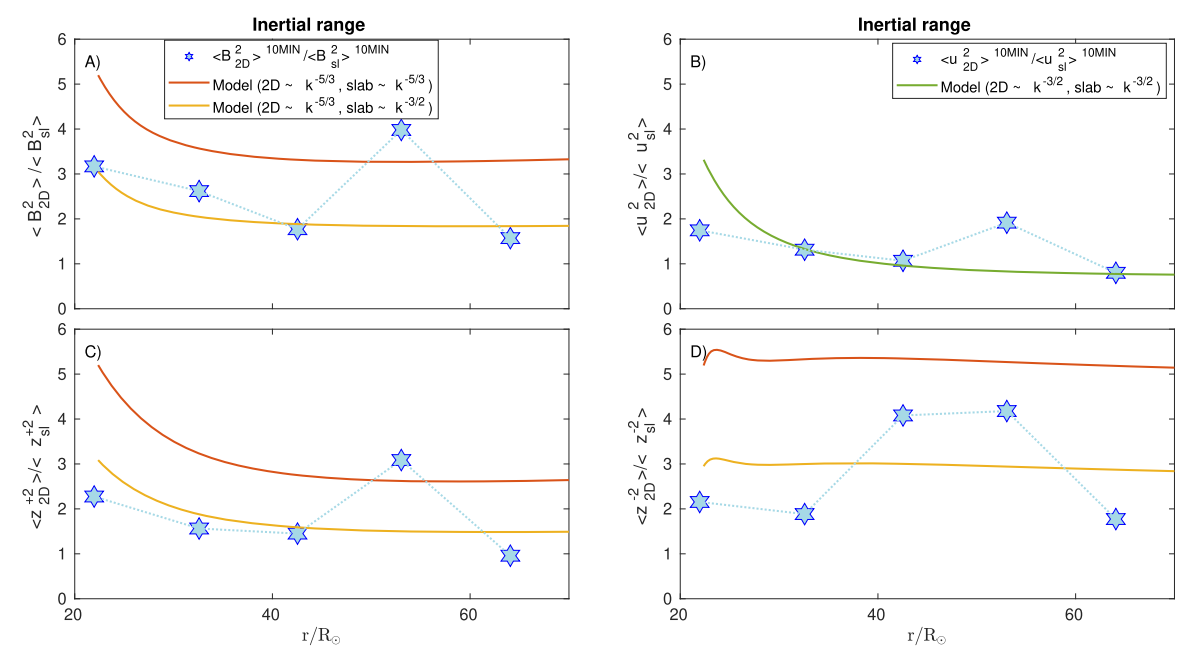


Figure 3. Comparison of the theoretical (solid curves) and observed ratio (blue stars/dotted curves) of the inertial range 2D and slab turbulence components as a function of distance in the inbound direction of PSP during encounters 1–9 of PSP. Panels (A)–(D) correspond to the fluctuating magnetic energy, fluctuating kinetic energy, outward Elsässer energy, and inward Elsässer energy. The solid orange curve assumes that the 2D and slab turbulence possess the same power-law form of $k^{-5/3}$. The solid yellow curve assumes that the 2D and slab turbulence exhibit a power law of $k^{-5/3}$ and $k^{-3/2}$, respectively.

Zank et al. 2017), in which the 2D component is the dominant component and the slab component is a minority component.

5. Discussion and Conclusions

The radial evolution of anisotropic turbulence as expressed in terms of magnetic field fluctuations, velocity fluctuations, and outward/inward Elsässer energy in the inertial range (and in the energy-containing range) was investigated for the inbound and outbound directions during encounters 1-9 of PSP between \sim 21 and 65 R_{\odot} , from a region closer to the Sun than those of previous studies (Bandyopadhyay & McComas 2021; Adhikari et al. 2022; Zhao et al. 2022). For this, we derived an equation describing the variance anisotropy for magnetic field fluctuations, velocity fluctuations, and inward and outward Elsässer energies in the inertial range. We used the Adhikari et al. (2017) approach, i.e., a dimensional analysis between the power spectra in the energy-containing and inertial ranges. In the energy-containing range, we assumed a $k^$ power law for the magnetic field fluctuations, velocity fluctuations, and inward and outward Elsässer energies. In the inertial range, for the magnetic field fluctuations, and the outward and inward Elsässer energies, we used two approaches: one in which both 2D and slab turbulence exhibit a Kolmogorov power law of $k^{-5/3}$, and the other in which the 2D and slab turbulence have different power laws of $k^{-5/3}$ and $k^{-3/2}$, respectively. For the velocity fluctuations, we assumed that both 2D and slab components follow a $k^{-3/2}$ power law. As the inertial range variance anisotropy equations contain the energy-containing range 2D and slab turbulence energies and correlation lengths, we obtained them by numerically solving the SW + NI MHD turbulence transport model equations (Zank et al. 2017; Adhikari et al. 2022). We compared the theoretical result of the ratio between 2D and slab fluctuating magnetic energy, fluctuating kinetic energy, and outward/ inward Elsässer energy in the inertial range with the

corresponding observed results derived from the PSP measurements. We summarize our findings as follows.

- 1. In the inbound direction during the PSP encounters 1–9 between \sim 21 and 65 R_{\odot} , the total number of θ_{UB} values computed over 4 hr long intervals is 274. Among these, 21 (7.66%) fall within the range of [65°–115°], and 160 (58.39%) fall within the range of [0°–25°] or [155°–180°]. Similarly, the total number of θ_{UB} values derived over 10 minute long intervals is 3843, with 396 (10.3%) falling in the [65°–115°] range, and 1660 (43.19%) falling in the [0°–25°] or [155°–180°] range.
- 2. In the outbound direction, the total number of θ_{UB} values derived over 4 hr long intervals is 184, with 15 (8.15%) falling in the $[65^{\circ}-115^{\circ}]$ range, and 101 (54.89%) falling in the $[0^{\circ}-25^{\circ}]$ or $[155^{\circ}-180^{\circ}]$ range. Likewise, for 10 minute long intervals, the total number of θ_{UB} values is 3840, with 453 (11.79%) falling in the $\theta_{UB} \rightarrow [65^{\circ}-115^{\circ}]$ range, and 1627 (42.23%) falling in the $\theta_{UB} \rightarrow [0^{\circ}-25^{\circ}]$ or $[155^{\circ}-180^{\circ}]$ range.
- 3. At a heliocentric distance of 0.18 au, a histogram of θ_{UB} corresponding to 10 minute long intervals displays a distribution of θ_{UB} spanning from 90°–170°, with a negative skewness of -1.47. However, when considering a 4 hr long interval, the histogram of θ_{UB} , with a skewness of -0.78, varies between 155° and 175°. This suggests that in certain instances, PSP may not observe 2D turbulence, as the background fields tend to exhibit a more radial orientation than an oblique one.
- 4. The transverse fluctuating magnetic energy, transverse fluctuating kinetic energy, and the transverse outward/inward Elsässer energy exhibit a maximum value near $\theta_{UB} = 90^{\circ}$, and a minimum value near $\theta_{UB} = 180^{\circ}$.
- 5. The transverse normalized cross helicity shows a minimum value near $\theta_{UB} = 90^{\circ}$, and a maximum value near $\theta_{UB} = 180^{\circ}$. Similarly, the transverse normalized

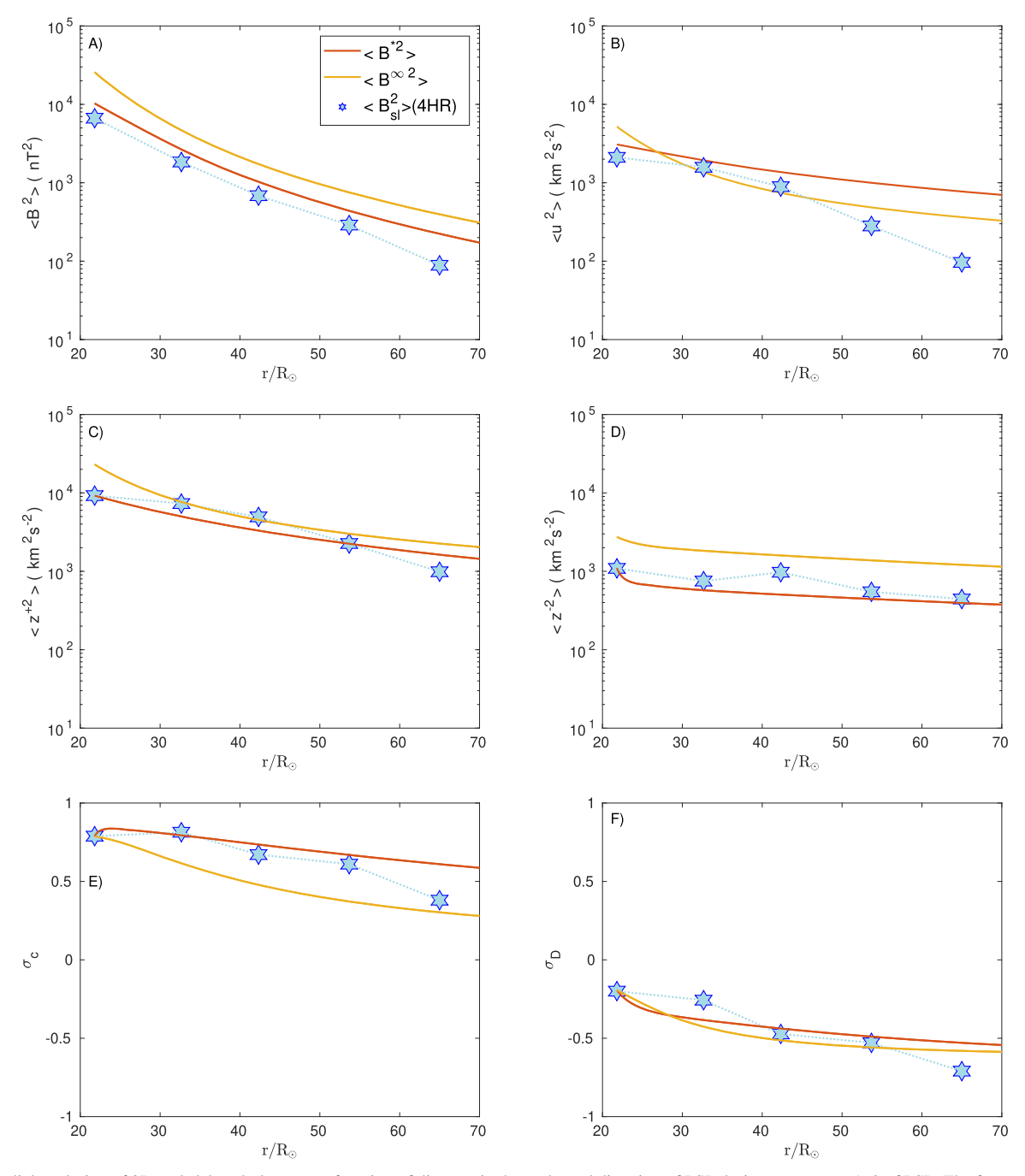


Figure 4. Radial evolution of 2D and slab turbulence as a function of distance in the outbound direction of PSP during encounters 1–9 of PSP. The format of the figure is similar to Figure 2.

- residual energy becomes more negative in the vicinity of orthogonal flows unlike when in the vicinity of radially aligned flows.
- 6. The theoretical and observed ratios of the inertial range 2D and slab fluctuating magnetic energies show good agreement with increasing distance in the inbound and outbound directions. These ratios in both directions exceed a value of 1, consistent with the expectations of ≪1 or *O*(1) plasma beta NI MHD theory (Zank & Matthaeus 1992a, 1992b, 1993). However, it is noteworthy that in the inbound direction, this ratio exhibits a larger value compared to the outbound direction, which may indicate that magnetic field fluctuations in the
- inbound direction were more anisotropic than those in the outbound direction.
- 7. The theoretical ratio of 2D and slab fluctuating kinetic energy reasonably agrees with the observed ratio in both inbound and outbound directions. In the inbound direction, the ratio exhibits a larger value compared to the outbound direction, which may also indicate that velocity fluctuations were more anisotropic in the inbound direction.
- 8. The theoretical and observed ratios of the inertial range 2D and slab energy in the outward/inward Elsässer energy are in agreement in both directions. In both cases, these ratios exceed 1, consistent with the NI MHD

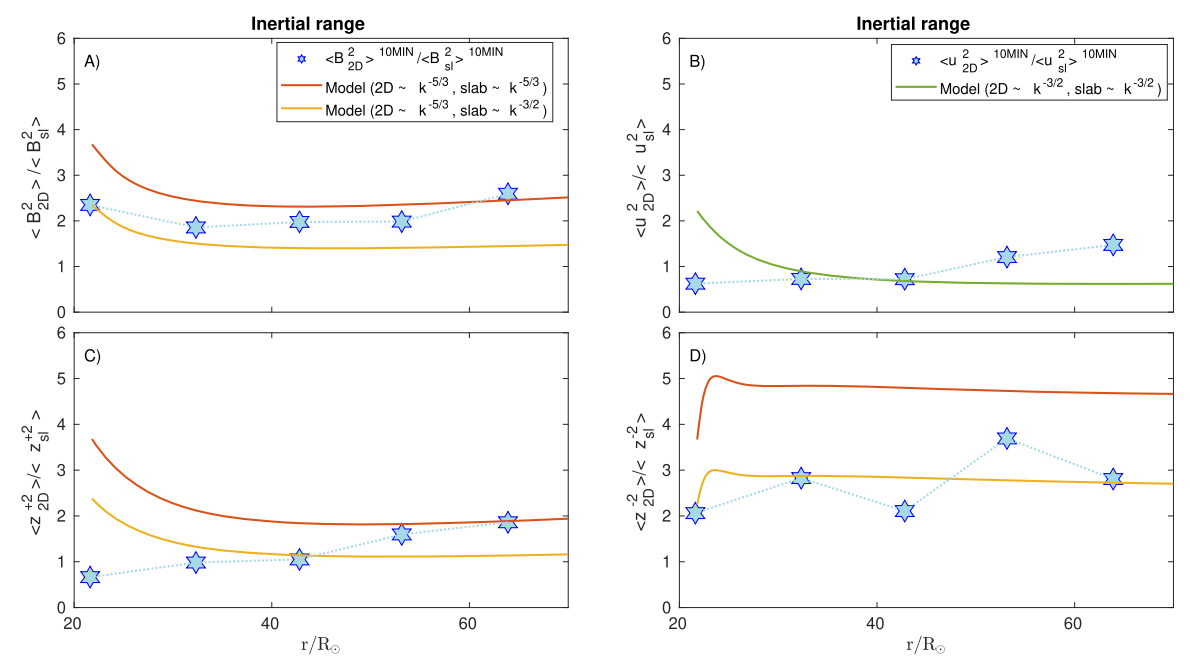


Figure 5. Comparison of the theoretical (solid curves) and observed ratio (blue stars/dotted curves) of the inertial range 2D and slab turbulence energies as a function of distance in the outbound direction during encounters 1–9 of PSP. The format of the figure is similar to Figure 3.

turbulence theory (Zank & Matthaeus 1992a, 1992b, 1993). The ratio in the inbound direction exhibited a larger value compared to the outbound direction.

- 9. In the energy-containing range, the theoretical results of the NI/slab fluctuating magnetic energy, fluctuating kinetic energy, outward/inward Elsässer energy, and normalized cross helicity and residual energy are relatively close to those measured by PSP.
- 10. The theoretical variance anisotropy in the inertial range relating to the $k^{-5/3}$ and $k^{-3/2}$ power laws between 2D and slab turbulence exhibits a smaller value compared to assuming the same power law $k^{-5/3}$ between 2D and slab turbulence.

We find that solar wind fluctuations in the young solar wind, i.e., near the Sun, are predominantly 2D and not slab, consistent with previous findings from theoretical and observational studies (Zank & Matthaeus 1992b, 1993; Bieber et al. 1996; Zank et al. 2017; Adhikari et al. 2022). This conclusion is contrary to the prior results of Bandyopadhyay & McComas (2021) and Zhao et al. (2022), indicating that a closer analysis is warranted, possibly using the mode-decomposition analysis developed recently by Zank et al. (2023), which is distinct from both these analyses and that presented here. An intriguing prospect is to extend this analysis from the sub-Alfvénic region to the super-Alfvénic region, including distances up to 1 au. This will generate valuable insights into solar wind dynamics in a broader spatial range.

Acknowledgments

We acknowledge the partial support of PSP contract No. SV4-84017, an NSF EPSCoR RII-Track-1 cooperative agreement OIA – 2148653, and NASA awards 80NSSC20K1783 and 80NSSC21K1319, NASA Heliospheric Shield 80NSSC22M0164, and the SWAP instrument effort on the New Horizons project (M99023MJM; PU-A WD1006357),

with support from NASA's New Frontiers Program and the IMAP mission as a part of NASA's Solar Terrestrial Probes (STP) mission line (80GSFC19C0027). This research was supported partially by the International Space Science Institute (ISSI) in Bern, through ISSI International Team project No. 560.

ORCID iDs

Laxman Adhikari https://orcid.org/0000-0003-1549-5256
Gary P. Zank https://orcid.org/0000-0002-4642-6192
Lingling Zhao https://orcid.org/0000-0002-4299-0490
Bingbing Wang https://orcid.org/0000-0002-6000-1262
Bofeng Tang https://orcid.org/0000-0002-2261-6629
Daniele Telloni https://orcid.org/0000-0002-6710-8142
Alexander Pitna https://orcid.org/0000-0001-8913-191X
Katariina Nykyri https://orcid.org/0000-0002-6905-9487

References

```
Adhikari, L., Zank, G. P., Telloni, D., et al. 2017, ApJ, 851, 117
Adhikari, L., Zank, G. P., Zhao, L. L., & Telloni, D. 2022, ApJ, 933, 56
Bale, S. D., Goetz, K., Harvey, P. R., et al. 2016, SSRv, 204, 49
Bandyopadhyay, R., & McComas, D. J. 2021, ApJ, 923, 193
Belcher, J. W., & Davis, L., Jr 1971, JGR, 76, 3534
Bieber, J. W., Wanner, W., & Matthaeus, W. H. 1996, JGR, 101, 2511
Bruno, R., & Telloni, D. 2015, ApJL, 811, L17
Chen, C. H. K., Bale, S. D., Bonnell, J. W., et al. 2020, ApJS, 246, 53
Dasso, S., Matthaeus, W. H., Weygand, J. M., et al. 2008, ICRC (Mérida),
   1,625
Dasso, S., Milano, L. J., Matthaeus, W. H., & Smith, C. W. 2005, ApJL,
  635, L181
Horbury, T. S., Forman, M., & Oughton, S. 2008, PhRvL, 101, 175005
Kasper, J. C., Abiad, R., Austin, G., et al. 2016, SSRv, 204, 131
Kasper, J. C., Klein, K. G., Lichko, E., et al. 2021, PhRvL, 127, 255101
Matthaeus, W. H., Ghosh, S., Oughton, S., & Roberts, D. A. 1996, JGR,
   101, 7619
Milano, L. J., Dasso, S., Matthaeus, W. H., & Smith, C. W. 2004, PhRvL, 93,
  155005
Oughton, S., Matthaeus, W. H., Wan, M., & Osman, K. T. 2015, RSPTA, 373,
```

Pine, Z. B., Smith, C. W., Hollick, S. J., et al. 2020, ApJ, 900, 93

```
Podesta, J. J. 2009, ApJ, 698, 986
Smith, C. W., Vasquez, B. J., & Hamilton, K. 2006, JGRA, 111, 9111
Wang, B. B., Zank, G. P., Adhikari, L., & Zhao, L. L. 2022, ApJ, 928, 176
Wang, X., Tu, C., & He, J. 2019, ApJ, 871, 93
Weygand, J. M., Matthaeus, W. H., Dasso, S., et al. 2009, JGRA, 114, A07213
Zank, G. P. 2014, in Transport Processes in Space Physics and Astrophysics, ed. G. P. Zank (Berlin: Springer)
Zank, G. P., Adhikari, L., Hunana, P., et al. 2017, ApJ, 835, 147
Zank, G. P., & Matthaeus, W. H. 1992a, JPIPh, 48, 85
```

```
Zank, G. P., & Matthaeus, W. H. 1992b, JGR, 97, 17189
Zank, G. P., & Matthaeus, W. H. 1993, PhFl, 5, 257
Zank, G. P., Nakanotani, M., Zhao, L. L., Adhikari, L., & Telloni, D. 2020, ApJ, 900, 115
Zank, G. P., Zhao, L. L., Adhikari, L., et al. 2022, ApJL, 926, L16
Zank, G. P., Zhao, L. L., Adhikari, L., et al. 2023, ApJS, 268, 18
Zhao, L. L., Zank, G. P., Adhikari, L., & Nakanotani, M. 2022, ApJL, 924, L5
Zhao, L. L., Zank, G. P., Adhikari, L., et al. 2020, ApJ, 898, 113
```